JOURNAL OF COMPUTATIONAL PHYSICS 113, 155–164 (1994)

Application of the Spectral Multidomain Method to the Navier–Stokes Equations

G. DANABASOGLU* AND S. BIRINGEN

Department of Aerospace Engineering Sciences, University of Colorado, Boulder, Colorado 80309-0429

AND

C. L. STREETT

Theoretical Aerodynamics Branch, NASA Langley Research Center, Hampton, Virginia 23665

Received October 2, 1992

An application of the spectral multidomain method to the two-dimensional, time-dependent, incompressible Navier–Stokes equations is presented. The governing equations are discretized on a non-staggered, stretched mesh with a mixed finite difference/Chebyshev method and are integrated by a time-splitting procedure. The accuracy of the multidomain method is demonstrated for two different channel flow configurations, one with a backward-facing step and the other with a rectangular step.The method is then applied to the investigation of the effects of an isolated, two-dimensional roughness element on the spatial development of instability waves in boundary layers.

1. INTRODUCTION

Domain decomposition methods, particularly the multidomain approach, for solving fluid dynamics problems using spectral methods have gained significant attention in recent years. A comprehensive review of related investigations and of different solution procedures, including the spectral element method [10, 7], can be found in Canuto *et al.* [3]. The primary reason for the popularity of the multidomain procedure is its ability to consider each subdomain independently, allowing a different mesh resolution in each subdomain. Consequently, subdomains of the flow field containing regions of sharp gradients can have as many grid points as necessary, independent of the mesh resolution in the others. Therefore, the use of the multidomain method as opposed to a single domain approach may be especially suitable for complex geometries, such as the flow over a step. Such configurations have significant applications in computational fluid dynamics, e.g., in the numerical simulation of transition over aircraft wings where surface irregularities can be approximated as small surface roughness elements utilizing the multidomain method.

In the present work, the multidomain method, applied only along the wall-normal direction (defined as the direction perpendicular to the free stream velocity), is based on an influence matrix technique requiring the continuity of the variables and their first derivatives across the interfaces [9]. In particular, we focus on the accuracy and continuity of the interface conditions for two different channel flow configurations (Fig. 1), using a mixed finite difference/Chebyshev method to integrate the two-dimensional, time-dependent, incompressible Navier–Stokes equations [4, 5]. The flows over a backward-facing step and a rectangular step in a channel constitute excellent cases to test the accuracy of a numerical method because the reattachment length strongly depends on the Reynolds number of the flow. The application of the present method to more realistic fluid problems such as the investigation of the effects of a surface roughness element on the instability and transition of boundary layer flows is also presented.

2. GOVERNING EQUATIONS

We consider the incompressible Navier–Stokes equations in nondimensional form written as

$$\nabla \cdot U = 0, \tag{1a}$$

$$\frac{\partial U}{\partial t} + (U \cdot \nabla)\, U = -\nabla p + \frac{1}{\mathrm{Re}} \nabla^2 U. \tag{1b}$$

* Present address: National Center for Atmospheric Research, P.O. Box 3000, Boulder, CO 80307-3000.

0021-9991/94 $6.00

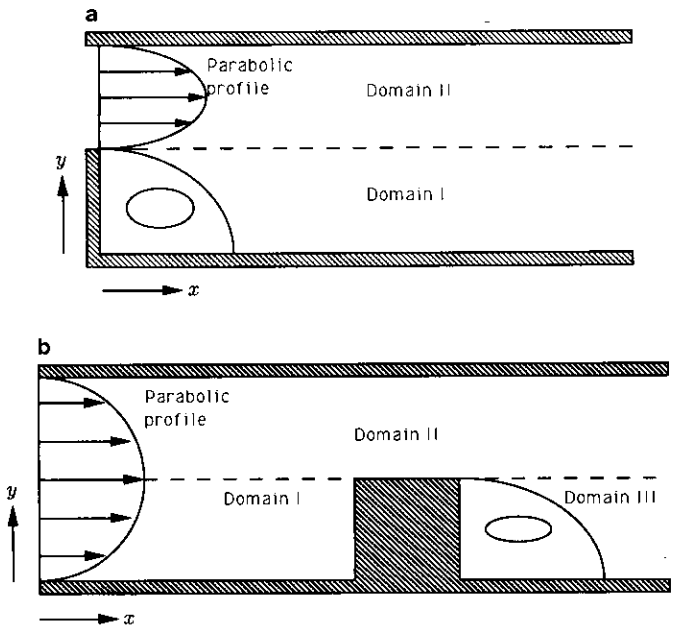

FIG. 1. Schematic of the flow (a) over a backward-facing step and (b) over a step in a two-dimensional channel. Dashed lines indicate domain interfaces.

In the above equations, $U=(u, v)$ is the velocity vector with streamwise (x) and normal (y) velocity components, respectively; t is time and p represents pressure. Also, Re is the Reynolds number defined as $\mathrm{Re}=u_m H/\nu$ and $\mathrm{Re}=u_\infty \delta_0^*/\nu$ for the channel flow and boundary layer configurations, respectively. Here, H is the channel height, u_m is the maximum velocity at inflow, δ_0^* is the boundary layer displacement thickness at inflow, u_∞ is the free stream velocity, and ν is kinematic viscosity.

For channel flows, the governing equations are integrated subject to the no-slip boundary conditions at solid boundaries. A fully developed parabolic velocity profile is prescribed at the inflow, and at the outflow, the computational domain is appended with a buffer domain in which the governing equations are modified to have strictly outgoing waves [5]. The buffer domain method enables the correct imposition of nonperiodic inflow–outflow boundary conditions required by spatially evolving flows and in separated flows where upstream effects are important.

In case of the boundary layer simulations, the above equations are written for the total velocity to obtain the steady state solutions for the base flow in the presence of a roughness element; the Blasius solution is used as the initial condition for these computations. This converged solution is then prescribed as the base flow for the instability simulations in which Eqs. (1a) and (1b) are written for the perturbation quantities. The perturbation equations are obtained by decomposing the flow variables into a steady base flow and a time-dependent component. For smooth plate simulations, the base flow is readily available from the solution of the Blasius equation.

Both the total and perturbation velocity equations are integrated subject to the no-slip boundary condition at solid boundaries. In all the simulations, the outer boundary of the computational domain extends upto 100 δ_0^*. At this far field boundary, the free stream conditions are applied. Consequently, the following relations were imposed for the total velocity and perturbation equations, respectively, at the outer boundary

$$u=1, \quad \frac{\partial v}{\partial y}=0 \quad \text{(total velocity)} \tag{1c}$$

$$u'=v'=0 \quad \text{(perturbation velocity).} \tag{1d}$$

In Eq. (1d), the primes denote the perturbation quantities.

For the total velocity equations, the inflow conditions consist of the Blasius profiles, whereas for the perturbation equations, a two-dimensional Tollmien–Schlichting (TS) wave is imposed at the inflow, so that

$$U'(x=0,\ y,\ t)=A_{2d}\Re[E_{\varepsilon 2d}e^{-i\omega_R t}]. \tag{2}$$

In Eq. (2), A_{2d} is the amplitude of the inflow perturbation velocities and $E_{\varepsilon 2d}=(u'_\varepsilon, v'_\varepsilon)$ is the complex velocity vector obtained from the spatial eigenfunctions of the Orr–Sommerfeld equation, corresponding to real frequency ω_R. Also, $i=\sqrt{-1}$ and $\Re[\ ]$ represent the real part of a complex number. Boundary layer simulations also incorporate the buffer domain method at the outflow.

3. SOLUTION PROCEDURE

The governing equations are discretized on a nonstaggered, stretched grid by using fourth-order central finite differences along the streamwise direction and by the Chebyshev collocation matrix method along the normal direction. The multidomain method can also be used with staggered grids and its application follows the approach described in this paper. A time-splitting procedure which uses the implicit Crank–Nicolson scheme for the normal direction diffusion terms is applied for time integration. All of the other terms are treated explicitly by a third-order, compact, low-storage Runge–Kutta method [11]. In order to satisfy the global mass conservation, the homogeneous Neumann boundary conditions for the pressure Poisson equation are converted to nonhomogeneous Dirichlet boundary conditions by the capacitance matrix method. The eigenvalue decomposition technique is then utilized to numerically integrate the Poisson equation with the Dirichlet boundary conditions. Grid points are smoothly clustered in the vicinity of the step. The computational procedure requires about 25 μs per time step per grid point on

the CRAY-2S at NASA Langley Research Center and is about twice as expensive as our previous single domain solver [5]. However, the current method is applicable to complex geometries with preserved spectral accuracy. The details of the numerical scheme are given in Danabasoglu [4].

3.1. Multidomain Method

In order to resolve the sharp flow field gradients in the vicinity of solid boundaries along the normal direction, the multidomain method [9] was implemented to divide the computational domain into several subdomains (Fig. 1) and the governing equations were integrated separately in each subdomain. In Figs. 1a and 1b, subdomain interfaces are denoted by dashed lines. Because subdomains may not necessarily coincide with the Chebyshev interval ($-1 \leqslant y \leqslant 1$), the application of the method requires the use of mapping functions along the normal direction; linear analytical functions were used for this purpose. Along the streamwise direction, fourth-order central finite differences are used on a stretched mesh in all the subdomains. At the corners, values of flow field variables are obtained from the solution in the upper subdomain (Fig. 1b) and because the finite difference discretization in lower subdomains does not require the corner values during the integration step, these values are unique.

In the subsequent parts of this section, the application of the multidomain method is illustrated by considering the one-dimensional model momentum equation. The application of the procedure to the Poisson/Laplace equations is also included.

3.1.1. *Multidomain Method for the Momentum Equations*

In the present work, because only the normal direction diffusion terms are treated implicitly, the discretized momentum equations reduce to one-dimensional systems. Therefore, the following example is sufficient to demonstrate the application of the method to the momentum equations. Let us consider,

$$\mathbf{G}V = RHS \qquad \text{for} \quad y \in [d, e]. \tag{3a}$$

Here, $\mathbf{G}$ is a coefficient matrix resulting from the discretization of the momentum equations, V is the vector of unknowns representing discrete values of u or v, and RHS is the right-hand-side vector. Equation (3a) is to be integrated subject to Dirichlet boundary conditions,

$$\begin{aligned} V(d) &= g_d, \\ V(e) &= g_e. \end{aligned} \tag{3b}$$

The boundaries are arbitrarily placed at d and e with $e > d$.

The multidomain method allows the subdivision of the computational domain into any number of subdomains. For sake of simplicity, we split the main integration domain into two arbitrary regions at $y = c$ with $d < c < e$. Consequently,

$$\text{Domain I}: [d, c],$$

$$\text{Domain II}: [c, e].$$

Point c is common to both regions and $V(c)$ is yet unknown.

The first step in the solution procedure consists of determining a solution that contains the influence of a unit disturbance at the interface point, requiring the integration of the following homogeneous systems of equations:

Domain I,

$$\mathbf{G}V_1^{\mathrm{I}} = 0, \tag{4a}$$

with

$$\begin{aligned} V_1^{\mathrm{I}}(d) &= 0, \\ V_1^{\mathrm{I}}(c) &= 1; \end{aligned} \tag{4b}$$

Domain II,

$$\mathbf{G}V_1^{\mathrm{II}} = 0, \tag{5a}$$

with

$$\begin{aligned} V_1^{\mathrm{II}}(c) &= 1, \\ V_1^{\mathrm{II}}(e) &= 0. \end{aligned} \tag{5b}$$

Here, subscript 1 stands for the first solution, and superscripts I and II refer to the first and second domains, respectively.

The second solution is obtained by integrating the nonhomogeneous system (Eqs. (3a)–(3b)) subject to a homogeneous Dirichlet interface condition:

Domain I,

$$\mathbf{G}V_2^{\mathrm{I}} = RHS, \tag{6a}$$

with

$$\begin{aligned} V_2^{\mathrm{I}}(d) &= g_d, \\ V_2^{\mathrm{I}}(c) &= 0; \end{aligned} \tag{6b}$$

Domain II,

$$\mathbf{G}V_2^{\mathrm{II}} = RHS, \tag{7a}$$

with

$$V_2^{II}(c) = 0,$$
$$V_2^{II}(e) = g_e. \tag{7b}$$

Once we have solutions 1 and 2 for each domain, because the system under consideration is a linear one, the total solution can be formed as

$$\text{Domain I: } V^I = V_2^I + \gamma V_1^I,$$
$$\text{Domain II: } V^{II} = V_2^{II} + \gamma V_1^{II}, \tag{8}$$

where γ is a constant to be determined from the interface condition.

The interface condition can be found by imposing the continuity of the solution at point c which requires

$$\frac{\partial V^I}{\partial y}(c) = \frac{\partial V^{II}}{\partial y}(c). \tag{9}$$

Because point c is common to both domains and there is only one value of γ, the function value at $y = c$ is unique. Substituting for the derivatives from Eqs. (8) into Eq. (9), we obtain

$$\gamma = \frac{\left[\dfrac{\partial V_2^{II}}{\partial y} - \dfrac{\partial V_2^I}{\partial y}\right]}{\left[\dfrac{\partial V_1^I}{\partial y} - \dfrac{\partial V_1^{II}}{\partial y}\right]}. \tag{10}$$

Once γ is known, the total solution can be calculated from Eqs. (8).

This solution method does not require any iterative procedure to find the interface value and the first solution is only a function of the geometry which can be calculated once in the first time step and used in the subsequent computations.

3.1.2. *Multidomain Method for the Poisson/Laplace Equations*

The application of the multidomain method to the Poisson/Laplace equations is more involved than its application to the momentum equations due to the multidimensionality of the problem. Let us consider the following elliptic equation

$$\mathscr{L}\mathbf{P} = \mathbf{RHS}, \tag{11a}$$

with nonhomogeneous Dirichlet boundary conditions. In this equation, **P** is the matrix of unknowns, **RHS** represents the right-hand-side matrix, and $\mathscr{L}$ is the two-dimensional discrete Laplace operator. The equation is integrated in the Cartesian domain defined as

$$x \in [a, b],$$
$$y \in [d, e],$$

with $b > a$ and $e > d$. Therefore, the boundary conditions can be written as

$$\mathbf{P}(a, y) = f_a(y),$$
$$\mathbf{P}(b, y) = f_b(y),$$
$$\mathbf{P}(x, d) = f_d(x),$$
$$\mathbf{P}(x, e) = f_e(x). \tag{11b}$$

Here, $f_a(y)$, $f_b(y)$, $f_d(x)$, and $f_e(x)$ represent arbitrary functions used as boundary conditions.

We start the process by dividing the integration domain into two subregions, defining an interface line at $y = c$ with $d < c < e$. Consequently, we obtain

$$\text{Domain I: } x \in [a, b],\ y \in [d, c],$$
$$\text{Domain II: } x \in [a, b],\ y \in [c, e].$$

First, we compute the influence of unit interface disturbances on the system and form an influence matrix. For this purpose, we consider a series of homogeneous equations,

Domain I,

$$\mathscr{L}\mathbf{P}_m^I = 0, \tag{12a}$$

with

$$\mathbf{P}^I(a, y) = \mathbf{P}^I(b, y) = \mathbf{P}^I(x, d) = 0,$$
$$\mathbf{P}^I(x, c) = \delta(\tau_m) \quad \text{on the interface for} \quad m = 1, 2, \ldots, N_r; \tag{12b}$$

Domain II

$$\mathscr{L}\mathbf{P}_m^{II} = 0, \tag{13a}$$

with

$$\mathbf{P}^{II}(a, y) = \mathbf{P}^{II}(b, y) = \mathbf{P}^{II}(x, e) = 0,$$
$$\mathbf{P}^{II}(x, c) = \delta(\tau_m) \quad \text{on the interface for} \quad m = 1, 2, \ldots, N_r. \tag{13b}$$

The above equations are solved for each interface point τ_m. In Eqs. (12) and (13), $\delta(\tau_m)$ (delta function) represents the unit interface disturbance, N_r is the number of interface

points excluding the boundary points, and m is the solution related to the mth interface point. Next, we calculate the residual vectors, R_m, which represent the discontinuity in the two solutions. These vectors must be eliminated to make the final solution continuous and are written as

$$R_m = \left(\frac{\partial \mathbf{P}^{\mathrm{I}}_m}{\partial y} - \frac{\partial \mathbf{P}^{\mathrm{II}}_m}{\partial y} \right), \tag{14}$$

forming the columns of the influence (residual) matrix, $\mathbf{R}$,

$$\mathbf{R} = [R_1, R_2, ..., R_{N_r}]. \tag{15}$$

In the above procedure, the only array that requires storage is $\mathbf{R}$, and the intermediate solutions can be overwritten.

The second step of the multidomain method requires the solution of the actual system,

$$\mathscr{L}\mathbf{P} = \mathbf{RHS}, \tag{16a}$$

with

$$\begin{aligned} &\mathbf{P}(a, y) = f_a(y), \\ &\mathbf{P}(b, y) = f_b(y), \\ &\mathbf{P}(x, d) = f_d(x), \\ &\mathbf{P}(x, e) = f_e(x). \end{aligned} \tag{16b}$$

Recalling that the computational domain contains two subdomains, the above system can be written as

Domain I,

$$\mathscr{L}\mathbf{P}^{\mathrm{I}} = \mathbf{RHS}, \tag{17a}$$

with

$$\begin{aligned} &\mathbf{P}^{\mathrm{I}}(a, y) = f_a(y), \\ &\mathbf{P}^{\mathrm{I}}(b, y) = f_b(y), \\ &\mathbf{P}^{\mathrm{I}}(x, d) = f_d(x), \\ &\mathbf{P}^{\mathrm{I}}(x, c) = 0; \end{aligned} \tag{17b}$$

Domain II,

$$\mathscr{L}\mathbf{P}^{\mathrm{II}} = \mathbf{RHS}, \tag{18a}$$

with

$$\begin{aligned} &\mathbf{P}^{\mathrm{II}}(a, y) = f_a(y), \\ &\mathbf{P}^{\mathrm{II}}(b, y) = f_b(y), \\ &\mathbf{P}^{\mathrm{II}}(x, c) = 0, \\ &\mathbf{P}^{\mathrm{II}}(x, e) = f_e(x). \end{aligned} \tag{18b}$$

Once $\mathbf{P}^{\mathrm{I}}$ and $\mathbf{P}^{\mathrm{II}}$ are calculated, the residual vector, R_r, is obtained from

$$R_r = \left(\frac{\partial \mathbf{P}^{\mathrm{I}}}{\partial y} - \frac{\partial \mathbf{P}^{\mathrm{II}}}{\partial y} \right). \tag{19}$$

Of course, because $\mathbf{P}(x, c) = 0$ are not the true interface conditions, R_r is not equal to zero. The true interface values are the ones which make the interface residuals zero. Consequently, by solving

$$\mathbf{R}R_t = R_r,$$

or

$$R_t = \mathbf{R}^{-1}R_r, \tag{20}$$

we obtain the true interface conditions, R_t.

Now, solving

Domain I,

$$\mathscr{L}\mathbf{P}^{\mathrm{I}} = \mathbf{RHS}, \tag{21a}$$

with

$$\begin{aligned} &\mathbf{P}^{\mathrm{I}}(a, y) = f_a(y), \\ &\mathbf{P}^{\mathrm{I}}(b, y) = f_b(y), \\ &\mathbf{P}^{\mathrm{I}}(x, d) = f_d(x), \\ &\mathbf{P}^{\mathrm{I}}(x, c) = R_t; \end{aligned} \tag{21b}$$

Domain II,

$$\mathscr{L}\mathbf{P}^{\mathrm{II}} = \mathbf{RHS}, \tag{22a}$$

with

$$\begin{aligned} &\mathbf{P}^{\mathrm{II}}(a, y) = f_a(y), \\ &\mathbf{P}^{\mathrm{II}}(b, y) = f_b(y), \\ &\mathbf{P}^{\mathrm{II}}(x, c) = R_t, \\ &\mathbf{P}^{\mathrm{II}}(x, e) = f_e(x), \end{aligned} \tag{22b}$$

gives the actual solution.

The application of the multidomain method to the solution of Poisson/Laplace equations with Neumann boundary conditions is very similar to the above procedure and is given in Danabasoglu [4].

4. RESULTS AND DISCUSSION

4.1. Application to the Poisson Equation

Before implementing the multidomain technique to the solution of the Navier–Stokes equations, we tested the accuracy of the method, especially the smoothness of

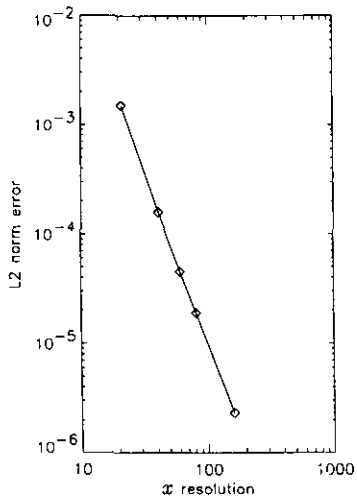

FIG. 2. L_2 norm error distribution for the model problem (Poisson equation) as a function of the x-direction mesh resolution.

the solution at domain interfaces, for an example problem consisting of the Poisson equation given as

$$\nabla^2 P = \left(\frac{\partial^2}{\partial x^2} + \frac{\partial^2}{\partial y^2}\right) P = -2\pi^2 \cos(\pi x)\cos(\pi y), \tag{23}$$

subject to homogeneous Neumann boundary conditions. In Eq. (23), P is the unknown function, and the integration domain is $0 \leqslant x \leqslant 2$ and $0 \leqslant y \leqslant 2$. The exact solution, P_e, for this model problem reads

$$P_e(x, y) = \cos(\pi x)\cos(\pi y). \tag{24}$$

Here, we set $y = 0.75$ as the interface line, and used 21 Chebyshev collocation points along the normal direction in both subdomains; along the x-direction, equally spaced grid points were used. In Fig. 2, the L_2 norm error is plotted as a function of the mesh resolution along the x-direction, showing the global accuracy of the solution method. Because the numerical scheme is reduced to second-order at the boundaries, the overall accuracy of the method is less than fourth order. The computational grid and the contours of P computed using 41 points along the x-direction are presented in Fig. 3, revealing the smoothness and continuity of the solution at the interface which is denoted by a dashed line. In Fig. 4, the interface distribution of the variable P is compared with the exact solution, showing excellent agreement. The distribution along the y-direction is identical to the distribution along the x-direction, atesting to the symmetry of the solution.

4.2. Application to the Navier–Stokes Equations

The first test problem we discuss in this section is the backward-facing step with a step height of $s = H/2$. Consequently, the computational domain can be conveniently divided into two equal subdomains (Fig. 1a). The numerical simulations were performed for Re = 150, 400, and 700; for Re = 150 and 400, the governing equations were integrated on a $21(y) \times 127(x)$ mesh in each subdomain with streamwise length of 6.5 in the physical domain. Also, at the outflow boundary, the length of the buffer domain was 3.6 with 24 grid points along x over this length. For Re = 700, the physical domain length was set to 12 with a resolution

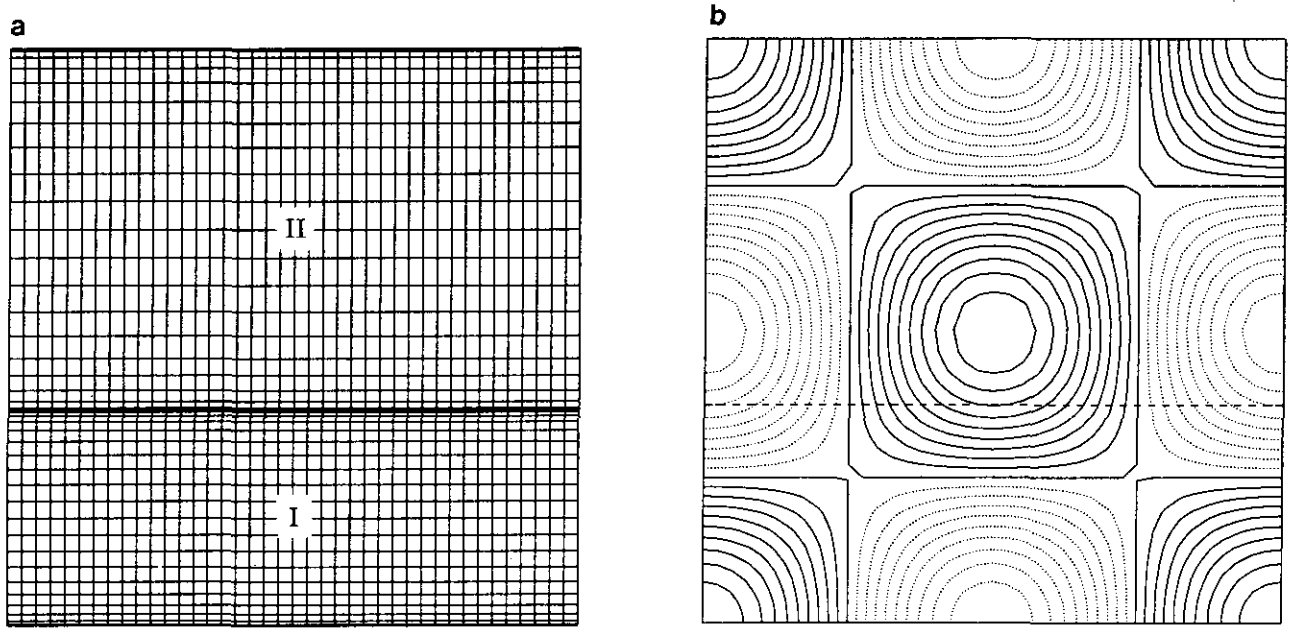

FIG. 3. (a) Computational grid ($21(y) \times 41(x)$ mesh in both subdomains) and (b) P contour plot for the model problem (contour interval (CI) = 0.1). The dotted lines indicate negative levels in related figures. The interface (dashed line) is at $y = 0.75$.

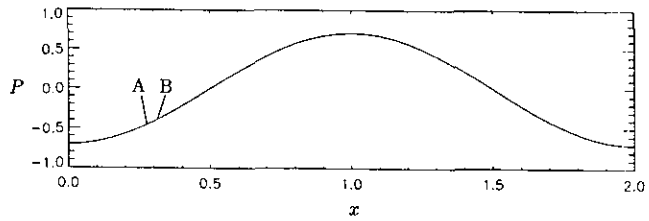

FIG. 4. Comparison of the numerical solution (A) with the exact solution (B) at the interface ($y = 0.75$) for the model problem.

of 21×172 grid points in each subdomain; the same buffer domain length was used for this case. The computational grid used in the latter simulations is displayed in Fig. 5.

The steady state reattachment lengths normalized by s for these three cases are presented in Table I and are compared with experimental measurements [1] and other numerical studies [1, 8, 2]. Accordingly, the present results display better agreement with the experimental measurements. In Figs. 6a–c, we give the contours of streamwise velocity, u, spanwise vorticity, ω_z, and velocity vectors at several streamwise locations for $\mathrm{Re} = 700$. In Fig. 6a, as a manifestation of high Reynolds number effects, the formation of a second separation bubble attached to the upper wall is clearly depicted. These figures also demonstrate the smoothness and continuity of the solution at the multidomain interface, thus lending evidence to the accuracy of the interface conditions.

As a second test problem, we considered the flow over a rectangular step placed in a two-dimensional channel (Fig. 1b). For this case, the parameters and the geometry were matched to the experimental conditions of Gackstatter [6] and Tropea and Gackstatter [12]. Consequently, the step height and length are equal to $H/2$ and $2H$, respectively, and $\mathrm{Re} = 162.6$. The governing equations were integrated in three subdomains (Fig. 7) with 21×95, 21×245, and 21×77 grids, respectively, in each subdomain. These grids resolve a total physical domain length extending for $0 \leqslant x \leqslant 10$. For this geometry, the buffer domain length was 3.8 with 34 grid points over this length.

The numerical simulations were continued until the solution reached a steady state. The results revealed a reattachment length of 4.8 (normalized by s) downstream of the step which is identical to the measured reattachment length obtained by Gackstatter [6]. The smoothness of the solutions revealed in the contour plots of u and ω_z (Figs. 8a and b) reaffirm the continuity and accuracy of the interface conditions. Finally, in Fig. 8c, velocity vectors plotted at several streamwise positions indicate that the flow preserves its initial parabolic velocity distribution until it accelerates near the step, where a jet-like behavior is observed.

TABLE I

Normalized Reattachment Lengths for the Flow over a Backward-Facing Step

Re	Present	Armaly *et al.*[a] [1]	Armaly *et al.*[b] [1]	Kim & Moin[c] [8]	Biringen & Kao[d] [2]
150	3.1	3.1	3.1	3.1	—
400	6.3	6.3	6.0	6.4	6.5
700	9.5	9.6	8.8	9.4	9.1

[a] Experimental measurements.
[b] 45×45 non-uniform mesh (streamwise length = 4 * reattachment length). For $\mathrm{Re} = 700$, a finer mesh was applied.
[c] 101×101 mesh (streamwise length = 15).
[d] 33×129 uniform mesh (streamwise length = 15).

4.3. Spatial Simulation of Boundary Layer Instability: Effects of Surface Roughness

In this section, we summarize the boundary layer instability simulations in which an isolated roughness element is placed downstream of the origin of disturbances at $x = 63.34$ with roughness height, $h_0 = 1.16$ (Fig. 9). Because the inflow boundary is placed at $\mathrm{Re} = 625.19$, the local Reynolds number at the roughness location is $\mathrm{Re} = 712.8$. Hence, the step height based on the local displacement thickness is $h = 1.01$. The length–height ratio of the step is set to 6.06:1, and $u_\infty/\nu = 4.4 \times 10^5\ \mathrm{m}^{-1}$. The free stream boundary is at $y = 101.16$. Also, the streamwise length of the physical domain is set to 161.92 and the buffer domain length is 40.

With this configuration, the Navier–Stokes equations were integrated on 21×217, 61×568, and 21×288 grids in the physical domain for subdomains I, II, and III, respectively, using the base flow and a disturbance field with $\omega_R = 0.0928$ as the initial and inflow conditions. Because this frequency is in the linearly unstable region for the Blasius flow, in the following discussion, it is referred to as the Tollmien–Schlichting (TS) frequency. The integration of the Orr–Sommerfeld equation for $\omega_R = 0.0928$ and $\mathrm{Re}_{\delta_0^*} = 625.19$ gives $\alpha = 0.24916 - i0.11643 \times 10^{-2}$, representing an unstable mode; here, α is the complex wave number. The

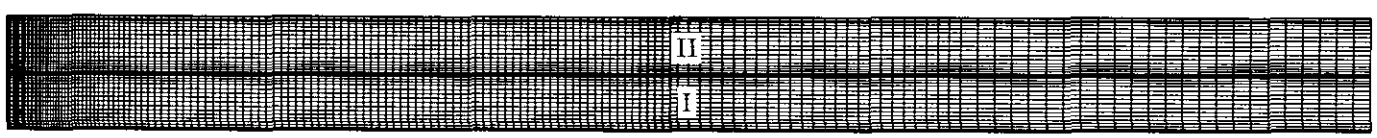

FIG. 5. Computational grid for the flow over a backward-facing step in a two-dimensional channel for $\mathrm{Re} = 700$. Each subdomain contains 21×172 grid points; the buffer domain is not included.

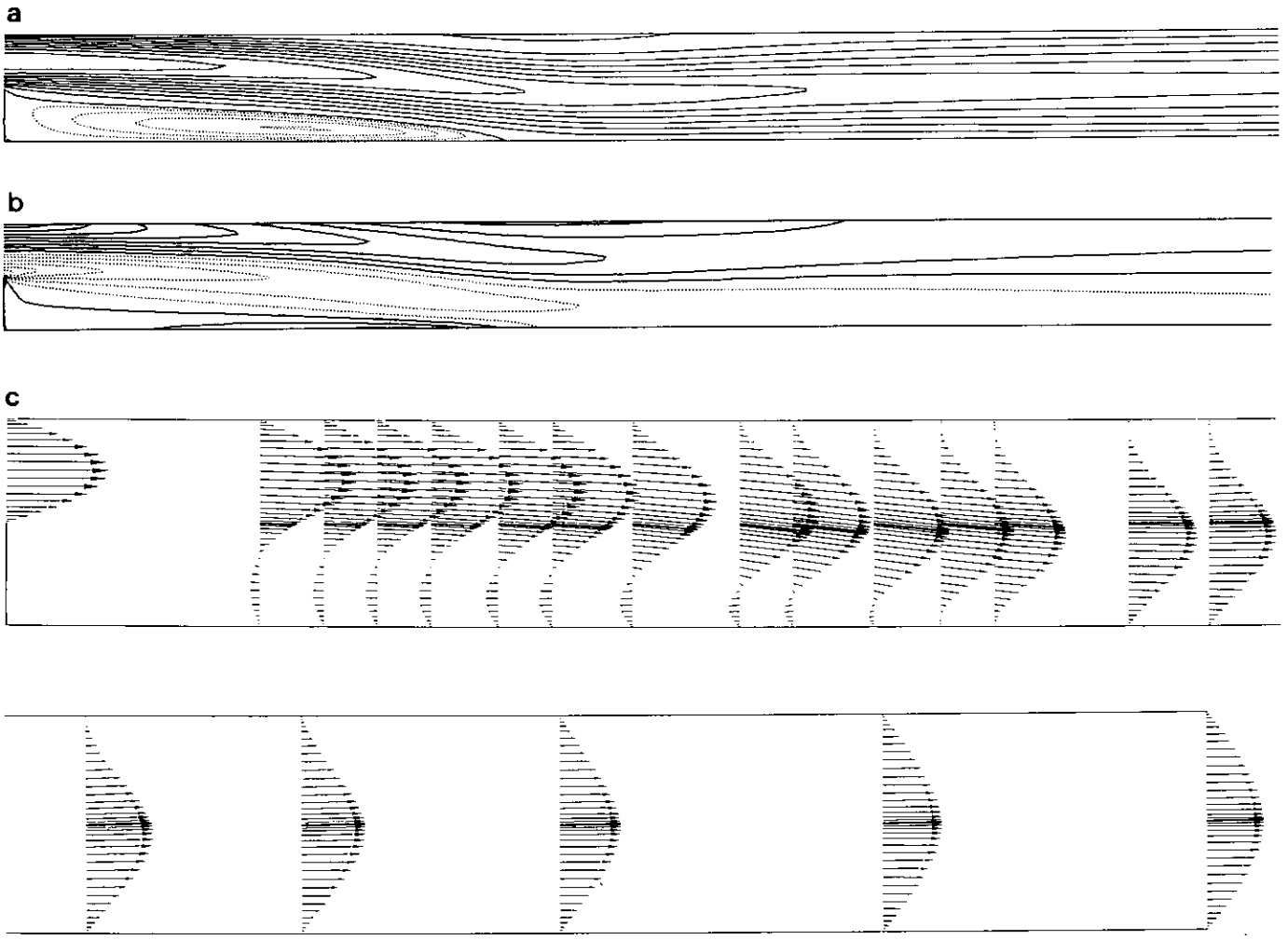

FIG. 6. Flow over a backward-facing step at Re = 700: (a) contour plot of u. Contour intervals are 0.03 and 0.1 for the negative and positive levels, respectively; (b) contour plot of ω_z (CI = 1.0); and (c) velocity vectors at $x = 0$, 1.25, 1.56, 1.82, 2.09, 2.41, 2.68, 3.07, 3.60, 3.86, 4.26, 4.59, 4.85, 5.51, 5.91, 6.80, 7.80, 9.00, 10.50, and 12.00. In (c), the bottom figure is the continuation of the top figure. Flow direction is from left to right.

streamwise length of the physical domain used in this simulation allows the resolution of about 6.5 TS wavelengths with a minimum of 60 grid points per wavelength. Also, during the integration, we set $A_{2d} = 0.0005$, and use 500 time steps per TS period.

The streamwise variation of $(u'_{\text{rms}})_{\max}$ is given in Fig. 10 (curve A); the distribution obtained from a smooth plate simulation with the same parameters is also shown in the figure for comparison purposes (curve B). Here, rms represents root-mean-square and max refers to maximum over y at a given x-location. The distribution with the roughness element deviates slightly from the smooth plate case in the region upstream of the roughness element. The presence of the element is manifested by a spike-like behavior at $x = 63.34$. After a slight decay over the element, the amplification in the separation zone is clearly observed.

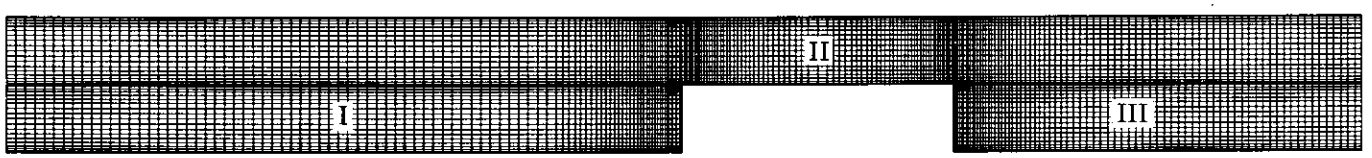

FIG. 7. Grid for the flow over a step in a two-dimensional channel for Re = 162.6. Each subdomain contains 21×95, 21×245, and 21×77 grid points, respectively; the buffer domain is not included.

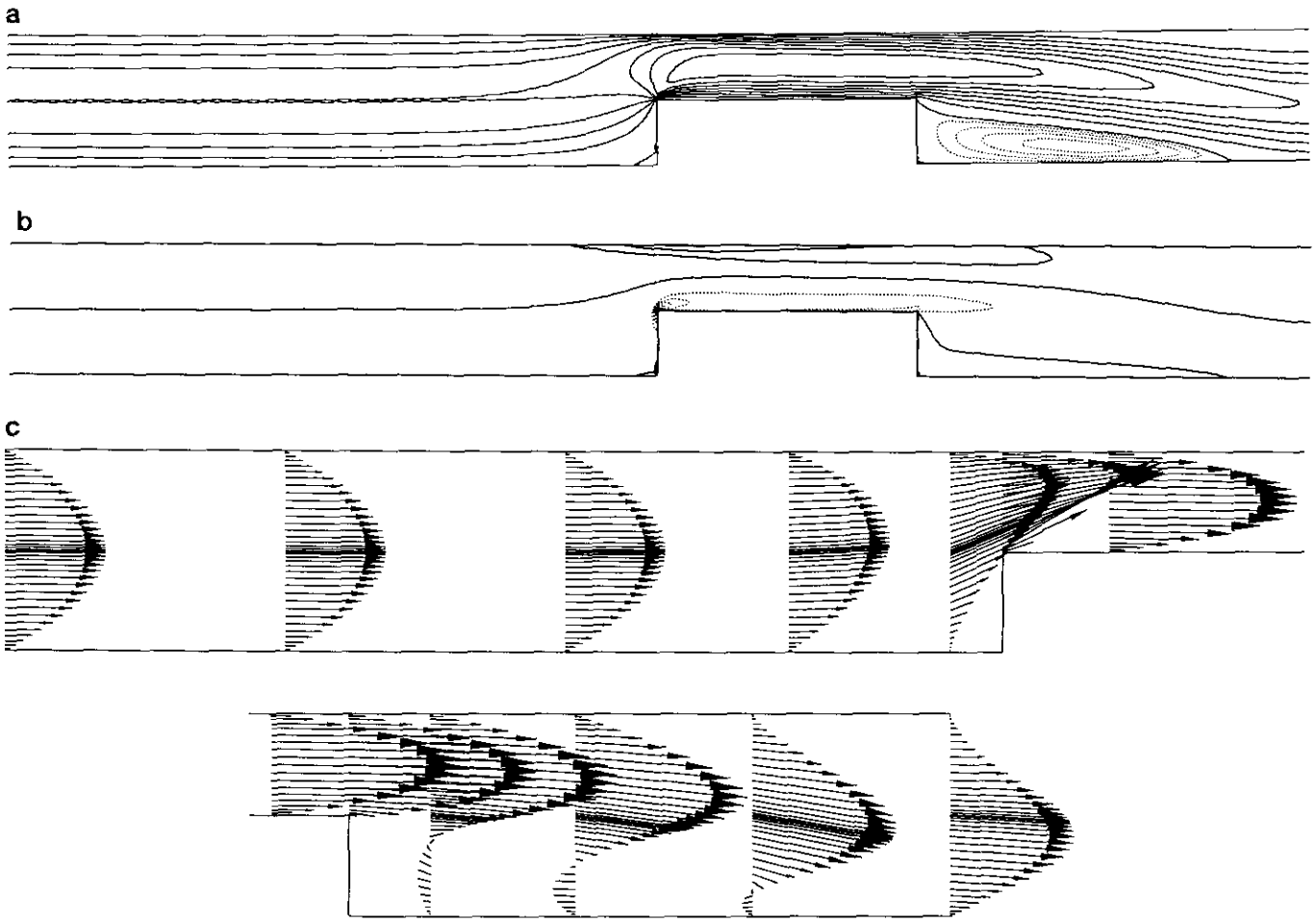

FIG. 8. Flow over a step at Re = 162.6: (a) contour plot of u. Contour intervals are 0.05 and 0.25 for the negative and positive levels, respectively; (b) contour plot of ω_z (CI = 7.5); and (c) velocity vectors at $x = 0$, 1.40, 2.80, 3.92, 4.73, 4.99, 5.52, 6.61, 6.99, 7.40, 8.13, 9.01, and 10.00. In (c), the bottom figure is the continuation of the top figure. Flow direction is from left to right.

We calculate the spatial growth rate of the disturbances as $\alpha_i \simeq -0.12$ in the region downstream of the roughness element, $77.42 \leqslant x \leqslant 91.32$, where growth is almost linear. This growth rate is significantly higher than the value predicted by the parallel linear stability theory, indicating that initially small amplitude disturbances attain finite amplitudes rapidly due to the amplifying effect of the roughness element.

In the subsequent simulation, we increase the perturbation frequency to $\omega_R = 0.1856$ which is stable for the Blasius flow; because this frequency is higher than the TS frequency for the Blasius flow, in the following discussion we will refer to this simulation as the inviscid frequency case. As before, the inflow conditions correspond to the eigenfunctions obtained from the Orr–Sommerfeld equation, using the

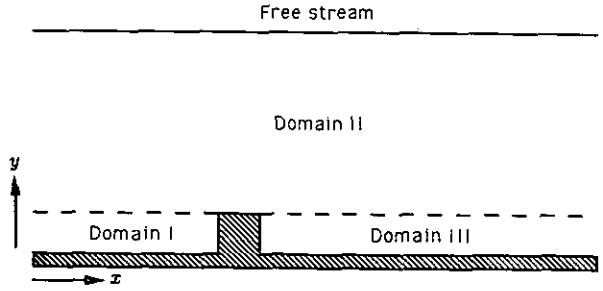

FIG. 9. Schematic of the two-dimensional boundary layer with an isolated roughness element. Dashed lines indicate domain interfaces.

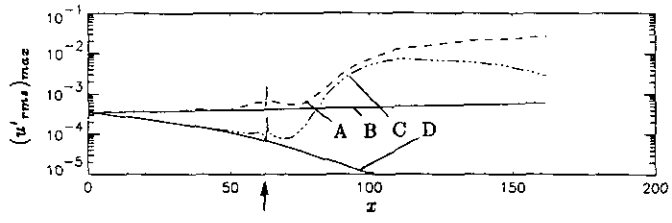

FIG. 10. Streamwise distributions of $(u'_{rms})_{max}$: with roughness, $\omega_R = 0.0928$ (A); without roughness, $\omega_R = 0.0928$ (B); with roughness, $\omega_R = 0.1856$ (C); and without roughness, $\omega_R = 0.1856$ (D). Roughness element is located at $x = 63.34$ indicated by an arrow.

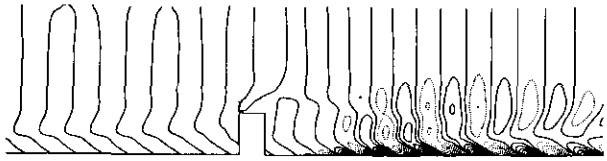

FIG. 11. Contour plot of ω_z' (CI = 0.005) for $\omega_R = 0.1856$. Normal direction is stretched by a factor of 10. Negative levels are indicated by dotted lines. Flow direction is from left to right.

Blasius profile which yields a stable mode with $\alpha = 0.44812 + i0.18925 \times 10^{-1}$ for $\omega_R = 0.1856$. For this simulation, about 13 wavelengths of the fundamental disturbance are resolved along the streamwise direction with 35 grid points per wavelength. The amplitude of the perturbations is kept at $A_{2d} = 0.0005$.

Figure 11 presents the contour plot of spanwise perturbation vorticity, ω_z', obtained after 26 TS periods and demonstrates that the disturbances are amplified in the separation zone and attain finite amplitudes rapidly in a short streamwise distance; farther downstream, the disturbance amplitudes attenuate slightly. In the smooth plate simulations without the roughness element, using the same initial conditions, the disturbances generated by this high frequency forcing rapidly decay.

The x distribution of $(u'_{\text{rms}})_{\max}$ for the inviscid frequency case is presented also in Fig. 10 (curve C) along with the TS frequency case (curve A) for comparison purposes. In accordance with the parallel linear stability theory, the disturbances decay upstream of the roughness element; however, a significant growth is observed in the separation zone (curve C). The computed spatial growth rate in $77.42 \leqslant x \leqslant 91.32$ is $\alpha_i \simeq -0.19$, which is considerably higher than the value calculated for $\omega_R = 0.0928$. In Fig. 10, curve D represents the distribution obtained from the flat plate simulation. These results are in good agreement with the experiments of Boiko, Dovgal, Kozlov, and Shcherbakov [13].

5. CONCLUSIONS

The multidomain method was successfully applied to numerically integrate the two-dimensional, time-dependent, incompressible Navier–Stokes equations. The test cases consisting of flows over a step and a backward-facing step placed in a channel revealed excellent agreement with the experimental results. The distributions of flow variables displayed no discontinuities at the interfaces, lending evidence to the accuracy of the interface conditions and to the applicability of the spectral multidomain method to complex geometries.

In the presence of an isolated, two-dimensional roughness element placed in a boundary layer, the computed spatial growth rates are significantly higher than those predicted by the linear theory for both Tollmien–Schlichting (TS) frequencies and higher (inviscid) frequencies. However, the inviscid frequencies obtain higher spatial amplification rates compared to the TS frequencies, suggesting that disturbances growing in the separation zone have an inviscid character.

ACKNOWLEDGMENTS

This work was supported by NASA Langley Research Center under Grant NAG-1-1161 and by ONR under Grant ONR00014-91-J-1086.

REFERENCES

1. B. F. Armaly, F. Durst, J. C. F. Pereira, and B. Schönung, *J. Fluid Mech.* **127**, 473 (1983).
2. S. Biringen and K. H. Kao, *Int. J. Numer. Methods Fluids* **9**, 1235 (1989).
3. C. Canuto, M. Y. Hussaini, A. Quarteroni, and T. A. Zang, *Spectral Methods in Fluid Dynamics* (Springer-Verlag, New York, 1988).
4. G. Danabasoglu, Ph.D. thesis, Department of Aerospace Engineering Sciences, University of Colorado, Boulder, 1992.
5. G. Danabasoglu, S. Biringen, and C. L. Streett, *Phys. Fluids A* **3**, 2138 (1991).
6. R. Gackstatter, Diplomarbeit, Lehrstuhl für Strömungsmechanik der Friedrich-Alexander-Universität, Erlangen-Nürnberg, Germany, 1984.
7. G. E. Karniadakis, E. T. Bullister, and A. T. Patera, in *Proceedings, Europe–U.S. Conf. Finite Element Methods for Nonlinear Problems*, edited by P. Bergan and K. J. Bathe (Springer-Verlag, New York, 1986), p. 803.
8. J. Kim and P. Moin, *J. Comput. Phys.* **59**, 308 (1985).
9. M. G. Macaraeg and C. L. Streett, *Appl. Numer. Math.* **2**, 95 (1986).
10. A. T. Patera, *J. Comput. Phys.* **54**, 468 (1984).
11. C. L. Streett and M. Y. Hussaini, ICASE Report No. 86-59, 1986 (unpublished).
12. C. D. Tropea and R. Gackstatter, *J. Fluids Eng.* **107**, 489 (1985).
13. A. V. Boiko, A. V. Dovgal, V. V. Kozlov, and V. A. Shcherbakov, *Fluid Dynamics* **25**, 12 (1990).